Adaptive Artifact Removal for Selective Multistatic Microwave Breast Imaging Signals

M. A. Elahi[a,*], M. Glavin[a], E. Jones[a], M. O'Halloran[a]

[a] *Electrical and Electronic Engineering*
National University of Ireland Galway

Abstract

Microwave imaging is one of the most promising alternative breast imaging modalities. Early-stage artifact removal is an important signal processing component of a microwave breast imaging system. In this paper, a monostatic artifact removal algorithm is extended to remove the early-stage artifact from multistatic radar signals. The multistatic radar signals exhibit greater variation in the early-stage artifact due to varying propagation paths between transmitting and receiving antennas. This variation makes it more challenging to estimate and remove the artifact compared to the monostatic signals. This paper proposes an entropy-based adaptive method to group signals with similar artifacts and then remove the artifact from each group separately using a hybrid artifact removal algorithm. The efficacy of the proposed algorithm has been demonstrated by imaging anatomically and dielectrically realistic 3D numerical breast phantoms.

Keywords: Microwave Imaging, Ultra Wideband Radar, Breast Cancer, Multistatic Artifact Removal, Skin Subtraction, Skin-Artifact Removal

1. Introduction

Confocal Microwave Imaging (CMI) systems for breast cancer detection require two stages of processing: early-stage artifact removal and image reconstruction [1]. The early-stage artifact is typically composed of the incident wave, combined with the reflection from the skin-breast interface and some residual antenna reverberation. If artifact is not effectively removed, it could mask any tumours present within the breast. Most artifact removal algorithms remove the artifact from a particular channel by estimating the artifact signal from the other channels. The variation between signals received at other channels greatly affect the ability of algorithm to produce an accurate estimate of the artifact. A comprehensive comparison of early-stage artifact removal algorithms

*Corresponding author
Email address: m.elahi1@nuigalway.ie (M. A. Elahi)

for microwave imaging of breast has been presented in [2]. The main conclusions from the study are that algorithms such as the average and the rotation subtraction method do not work well when there is a variation between channel artifacts. Conversely, filter-based methods are more robust to the variation in between-channel artifacts, but the window containing the artifact must be known *a-priori*. The entropy-based method estimates the window containing the artifact, but often introduces distortion into the tumour response.

A Hybrid Artifact Removal (HAR) algorithm has been proposed in [3], which combines the entropy-based approach and the Wiener filter algorithm to effectively remove the artifact while preserving the tumour response. The HAR algorithm has shown robustness to the variation in the artifacts but it has only been tested in monostatic scenarios. The variation in the monostatic signals is primarily due to the variation in the skin shape and the skin thickness. In contrast, the multistatic signals exhibit greater variation not only due to the varying skin shape and the thickness but also due to the different propagation distance between transmitting and receiving antenna. Most of these artifact removal algorithms have been solely used with monostatic radar signals, with the exception of the rotation subtraction algorithm [4]. However, the rotation subtraction algorithm is specific to the geometry of hardware prototype for breast cancer imaging reported in [4]. In this paper, a novel multistatic artifact removal (MAR) algorithm is proposed. The proposed algorithm extends the HAR algorithm used for monostatic signals [3] to the more challenging scenario of multistatic signals. In the HAR algorithm, the artifact-dominant portion of the signals is estimated using the entropy-based approach and the artifact is then removed by a Wiener filter. In the multistatic artifact removal alogrithm, the signals containing similar early-stage artifacts are adaptively grouped together based on the entropy-based method, and each group is separately processed through the HAR algorithm in order to remove the artifacts while preserving the tumour response. The MAR algorithm allows inclusion of multistatic signals in the imaging in addition to the monostatic signals. The combined monostatic and multistatic (CMM) imaging approach improves the imaging quality compared to monostatic-only imaging approach. The block diagram of the proposed

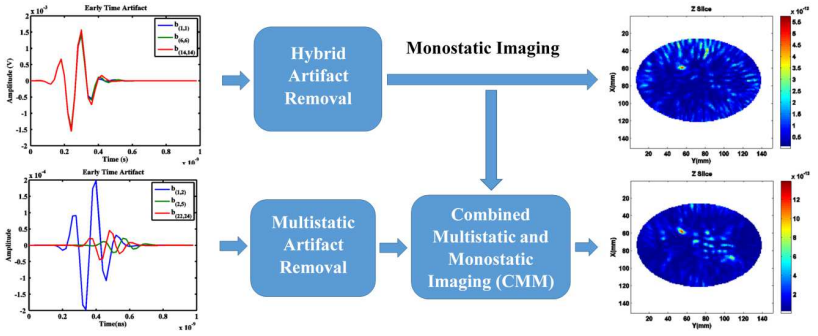

Figure 1: Block diagram of the proposed method

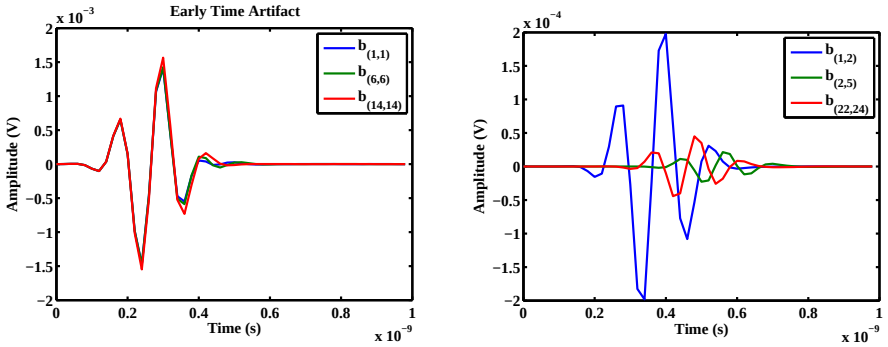

(a) Monostatic signals (b) Multistatic signals

Figure 2: Early-time part of time-domain backscattered radar signals (first 50 time samples shown). $b_{(i,j)}$ is the backscattered signal recorded at antenna j, where i is the index of the transmitting antenna, j is the index of the receiving antenna.

method is shown in Fig. 1. The algorithm is evaluated using anatomically and dielectrically accurate 3-D Finite-Difference Time-Domain (FDTD) breast models and a range of appropriate performance metrics.
The remainder of the paper is organised as follows: Section 2 describes extension of the hybrid algorithm to multistatic artifact removal; Section 3 describes experimental setup and 3D numerical breast phantoms; Section 4 details various tests applied to the artifact removal algorithm and corresponding results; finally, conclusions and suggestions for possible future work are discussed in Section 5.

2. Multistatic Artifact Removal

The general assumption about the musltistatic signal acquisition approach is that an increased number of radar signals provide more information about strong scatterers present within the breast. However, the improvement in the multistatic images may not be incremental as each additional multistatic signal is added [5, 6]. The selection of good quality multistatic signals for multistatic imaging can significantly improve the overall imaging provided the early-stage artifacts can be effectively removed.

The HAR algorithm has shown promising results when applied to monostatic signals due to the similarity of the monostatic artifact in all channels (Fig. 2 (a)). However, it cannot be directly applied to the multistatic signals due to greater variation in the artifact (Fig. 2 (b)). The channel to channel variation in artifact depends upon the propagation path of the signal between the transmitting and the receiving antennas, which makes it more challenging to estimate and remove the artifact. However, it is possible to identify and group the multistatic signals having similar artifacts so that the HAR algorithm can be separately applied to each group.

The performance of HAR is dependent on the degree of similarity between the signals in each group, which may vary across all signal groups. This is due to the fact that the Wiener filter estimates the artifact in a particular channel based on the artifact present in all other channels. If there is greater variation in the artifacts in the other channels, the estimated artifact will be less accurate. The greater variation in the artifacts also affects the artifact-dominant time-window estimation. Therefore it may not be possible to effectively remove the artifact from each signal group and it is important to adaptively select only those signal groups where the artifact can be effectively removed in order to achieve better quality images.

2.1. Signal Grouping Method

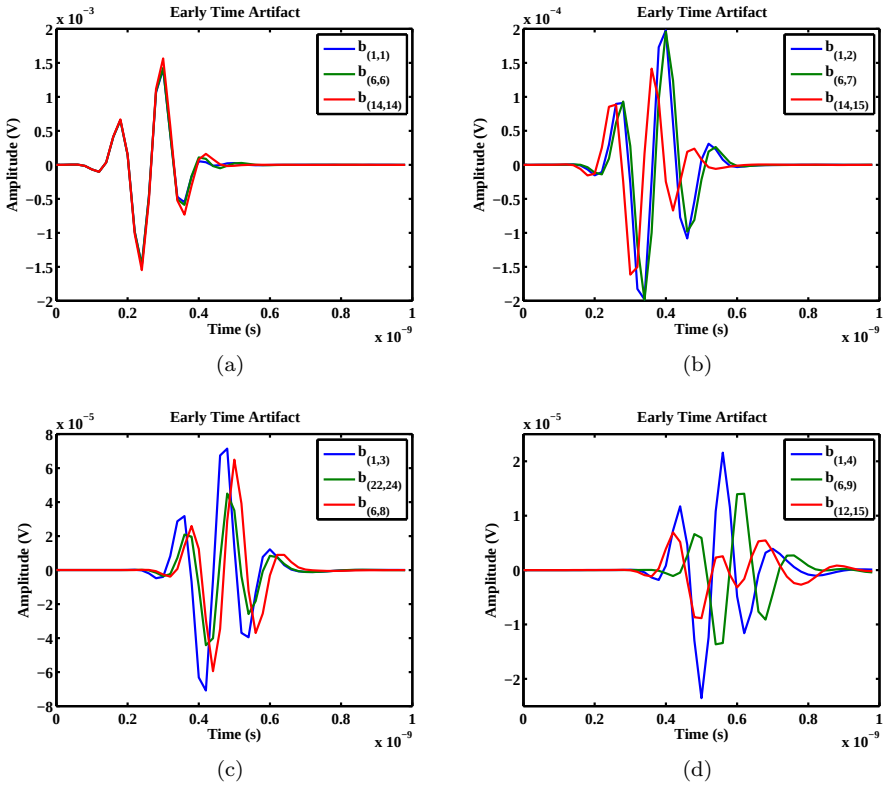

Figure 3: Early-time part of time-domain backscattered radar signals (first 50 time samples shown): (a) the monostatic siginals; (b) the signals of the form $b_{(i,i+1)}$; (c) the signals of the form $b_{(i,i+2)}$; (d) and the signals of the form $b_{(i,i+3)}$

The signal grouping is based on the spacing between the transmitting and receiving antenna pair. The initial signal grouping is similar to the grouping described in [6]. Let $b_{(i,j)}$ be the backscattered signal recorded at antenna j,

where i is the index of the transmitting antenna, j is the index of the receiving antenna, $i = 1, ..., N$, $j = 1, ..., N$ and N is the total number of antennas in the array. The signals of the form $b_{(i,i)}$ are the monostatic signals with similar early-time artifacts, and therefore can be combined into one group. The early-time artifact is expected to be also similar for the signals of the form $b_{(i,i+k)}$ and $b_{(i+k,i)}$ where $i + k \leq N$ and i is the index of the transmitting antenna, hence a total number of L groups can be formed [6].

The similarity between signals in each group is dependent on the spacing between transmitting and the receiving antenna pair and the distance from the skin. For example, the transmitting-receiving antenna pair $(1, 2)$ and $(6, 7)$ have identical spacing and a common distance from the skin. Therefore the skin-artifact in the signals $b_{(1,2)}$ and $b_{(6,7)}$ is similar, as shown in Fig. 3b. It can be seen that the degree of similarity between signals of the form $b_{(i,i+1)}$ is not identical but very similar to the monostatic signals whereas it decreases with increasing k, as shown in Fig. 3c (where $k = 2$) and Fig. 3d (where $k = 3$). This decrease in similarity can be attributed to increased spacing between the transmitting-receiving antenna pairs and the varying shape of the breast with increasing k. The decrease in similarity directly effects the performance of the HAR algorithm which is independently applied to each signal group.

2.2. Adaptive Signal Selection

The authors propose an entropy-based method to adaptively select the useful signal groups from a total of L groups and signals within each group, in order to achieve better Signal-to-Clutter (S/C) ratio in the resultant multistatic images compared to a monostatic image formation approach. In the proposed algorithm, entropy is used to measure the degree of similarity between signals within each group, and compared with other groups in order to select useful multistatic signals. The similar artifacts in the early portion of the radar signals result in a larger value of entropy, whereas much lower entropy values are obtained from the tumour reflections. The $\alpha-order$ Renyi entropy [7] is defined as:

$$H_\alpha[n] = \frac{1}{1-\alpha} log \left\{ \sum_{i=1}^{Q} \left(p_i[n]\right)^\alpha \right\} \tag{1}$$

where α is a real-positive, $p_i[n]$ is the normalized probability density function created by normalizing each radar signal within each group and Q is the total number of signals within the group. The entropy changes from $log\ Q$ (for similar early-time signals) to zero (for variations in late-time signals). Third-order entropy is typically defined for a broad class of signals [8], therefore $\alpha = 3$ is used in this study. Theoretical dimension of $[b_1[n], b_2[n], ..., b_Q[n]]$ is defined as:

$$D[n] = e^{H^s_\alpha[n]} \tag{2}$$

where $H^s_\alpha[n]$ is the smoothed entropy, obtained by applying a smoothing window to (1).

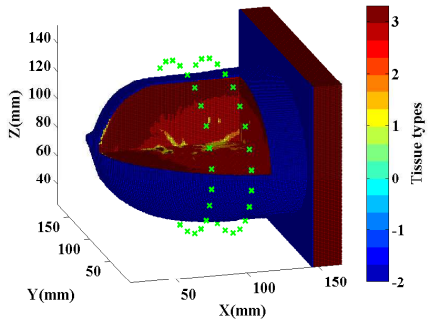

Figure 4: 3D FDTD model showing the breast and the antenna array. Each color represents a tissue type.

$D[n]$ provides the degree of similarity between signals within a group of signals [9]. As expected, the highest degree of similarity is exhibited by the monostatic signals. Therefore, computed $D[n]$ for monostatic signals is used as a benchmark to decide if the degree of similarity between signals in each group is sufficient to effectively remove the artifact from each group. The $D[n]$ for each subsequent signal group is then computed and correlated with the $D[n]$ of the monostatic signals group. The signal groups with correlation coefficient above a specific threshold are selected (with the threshold chosen empirically), whereas the remaining groups are ignored. The signals included within each group of the form $b_{(i,i+k)}$ and $b_{(i+k,i)}$ is also decided on the basis of the correlation coefficient. Any signal negatively affecting the correlation coefficient of that specific group is excluded from the group, and hence only a subgroup of the multistatic signals is selected for use in the image formation process. Once the signal groups and the signals within each group have been selected, each group is separately processed through the HAR algorithm to remove the artifact. Finally the artifact removed signals are processed through the beamforming algorithm to produce the final breast image.

3. Experimental Setup and Performance Metrics

The breast models and the antennas used are simulated using the FDTD method. The numerical breast models used in this study are based on the MRI-derived breast phantoms available from UWCEM MRI breast cancer repository [10]. These MRI-derived breast models are anatomically realistic and provide realistic heterogeneity as well as realistic distribution of various tissues within the breast. The dielectric properties of normal and malignant breast tissues are incorporated using Debye models and are based on the studies by Lazebnik *et. al.* [11].

An antenna array consisting of two rings of Hertizian dipole antennas is positioned around the breast. Each antenna ring contains 25 antenna elements and each antenna is placed at approximately constant distance from the skin

as shown in Fig. 4. Each antenna transmits a 6.0 GHz differentiated Gaussian pulse with a -3dB bandwidth of 5 GHz and a backscattered waveform is recorded at each of the antenna in the array.

Four breast models with different degree of radiographic density have been considered. A 15mm tumour model is placed at different locations within each breast model. Table 1 describes the radiographic density of each breast model and corresponding tumour locations.

Table 1: Description of Breast Models

	Label	Breast Density	Tumour Location
1	M0	Homogeneous fat	(60mm, 55mm, 80mm)
2	M1	mostly fat (<25% glandular tissue)	(55mm, 60mm, 65mm)
	M2		(85mm, 105mm, 70mm)
	M3		(60mm, 55mm, 90mm)
3	M4	scattered fibroglandular (25-50% glandular tissue)	(45mm, 50mm, 105mm)
	M5		(88mm, 70mm, 105mm)
4	M6	heterogeneously dense (51-75% glandular tissue)	(60mm, 110mm, 70mm)

The performance of the artifact removal and the imaging process has been evaluated using three performance metrics. The Peak-to-Peak Response Ratio (PPRR) is defined as the ratio of the peak-to-peak magnitude of the artifact prior to the application of the artifact removal and following the artifact removal. The PPRR is applied to the raw signals and it quantifies the artifact removal from a particular channel. The PPRR independently evaluates the performance of the artifact removal algorithm. The Signal-to-Mean Ratio (S/M) and Signal-to-Clutter ratio (S/C) are computed from the reconstructed breast images. The S/C is defined as the ratio of the tumour energy to the strongest clutter energy in the image and it measures the quality of the reconstructed breast image. Finally, the S/M is defined as the ratio of peak tumour energy to the average energy within the reconstructed breast image.

4. Results

In order to demonstrate performance of the multistatic artifact removal algorithm and to compare the imaging results with the monostatic approach, both monostatic and multistatic backscattered signals are first obtained from the breast model M0 with tumour located at position (60 mm, 55 mm, 80 mm).

Fig. 5 shows the third-order entropy based function, $D[n]$, and the estimated artifact-dominant time-window for each of the signal groups containing

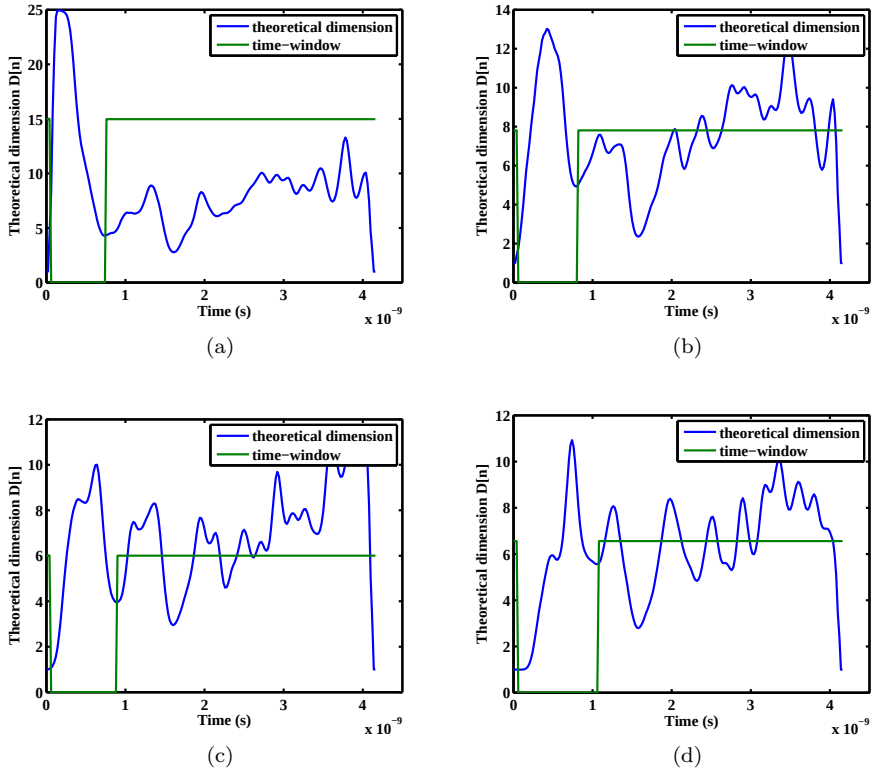

Figure 5: Theoretical dimension $D[n]$ and estimated artifact dominant time-window functions obtained from: (a) the monostatic signals group; (b) the multistatic group containing signals of the form $b_{(i,i+1)}$; (c) the multistatic group containing signals of the form $b_{(i,i+2)}$; (d) and the multistatic group containing signals of the form $b_{(i,i+3)}$

all signals of the form $b_{(i,i+k)}$ where $k = 0, 1, 2, 3$ and $k = 0$ is the monostatic group. The artifact-dominant time-window for each group is estimated using the *maxima-minima* approach [3]. The early-time artifact is present in the early-time part of the signal before any reflections from the interior of the breast. Therefore, the early-time part of the function D[n] is used to estimate the artifact-dominant time window. Firstly, the *maximum* of the function D[n] is computed. Next, the artifact-dominant time window is defined from the start of the signal to the location of the local *minimum* that: (a) is adjacent to the *maximum*; (b) follows the *maximum*; (c) and that is significantly lower than the *maximum*. It can be observed from Fig. 5a that there is a significant difference between the first *maxima* and the adjacent *minima* of $D[n]$ computed from the monostatic signals. However variation in $D[n]$ increases in the multistatic signals group with an increase in k (Fig.5b-5d).

The increased variation in $D[n]$ is indicative of a corresponding variance in

Algorithm 1 Pseudocode to estimate the artifact-dominant time window

```
n ← 1 : M/2
maximum ← maximum of D[n]
minima ← minima of D[n]
for each: minimum ∈ minima
 if minimum is adjacent to the maximum and
    minimum follows the maximum and
    minimum is significantly lower than the maximum then
     m_0 ← location of the minimum
     window ← 1 : m_0
 end if
```

multistaic signals. It becomes difficult to estimate the correct artifact-dominant time window based on the *maxima-minima* approach. The difficulty is obvious from a closely located *maxima-minima* in Fig. 5d. In order to obtain artifact free signals, each group of signals is separately processed through the Wiener filter, after the artifact-dominant time-window has been estimated for each group.

Time-domain signals obtained after artifact removal have been plotted in Fig. 6 (one from each signal group i.e for $k = 0, 1, 2, 3$). The corresponding ideal tumour signals are also shown for the comparison. The ideal tumour signals are produced by subtraction of the radar signals acquired from with-tumour and tumour-free homogeneous breast models. It can be observed from Fig. 6a- 6c that the early-stage artifact has been significantly reduced while the tumour response is preserved in the monostatic signals and multistatic signals of the form $s_{(i+k,i)}$, where $k = 1$. There is still some residual artifact that can be compensated for by incoherent addition at the beamforming stage. However, the residual artifact in the multistatic signals of the form $s_{(i,i+k)}$, where $k = 2$ is slightly greater compared to the monostatic group and the multistatic group with $k = 1$, and it is worst in the case of multistatic signals of the form $s_{(i,i+k)}$, where $k = 3$ (Fig. 6d).

The poor performance of artifact removal for the signals of the form $s_{(i,i+k)}$ where $k = 3$, can be attributed to the ambiguity in the artifact-dominant window estimation. Another factor is the poor artifact estimation by the Wiener filter due to greater variation among signals within this group. Therefore, the group containing signals of the form $b_{(i,i+k)}$ where $k \geq 3$ must be excluded from the image formation process. Inclusion of such groups will contribute negatively towards the S/C ratio in the final image. This information is not known prior to application of the artifact removal. However it can be predicted based on the entropy-correlation method proposed in Section 2. Fig. 7a shows the correlation coefficient (r) computed by the correlation of $D[n]$ of each multistatic signal group (for $k = 1, 2, 3$) with the $D[n]$ of the monostatic signals group. It can be seen that the highest correlation coefficient is obtained from signal groups containing signals of the form $b_{(i,i+k)}$ where $k = 1, 2$ and it significantly drops for $k > 2$. This correlates with the results shown in Fig. 5.

Hence the correlation coefficient can be used to limit the number of signal

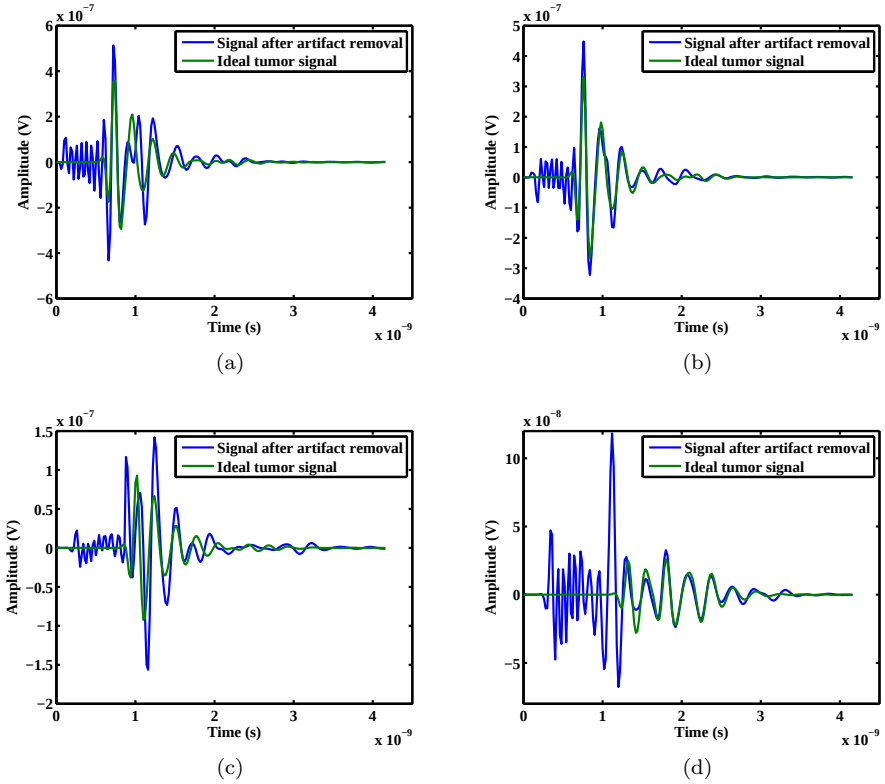

Figure 6: Time domain signals after artifact removal: (a) the monostatic signal $s_{(16,16)}$; (b) the multistatic signal $s_{(16,15)}$; (c) the multistatic signal $s_{(9,11)}$; (d) and the multistatic signal $s_{(3,6)}$.

groups that should be included in an image formation process in order to improve the S/C ratio. The Modified Delay-and-Sum beamformer (MDAS) is used to obtain the monostatic and the CMM images following the proposed artifact removal algorithm [12]. However, the artifact removal algorithm can be used with any beamformer.

The CMM images are generated by varying the threshold of the correlation coefficient shown in Fig. 7a and the image quality metrics (S/C and S/M) are computed from the resultant images. The S/C is plotted in Fig. 7b as a function of the total signals used to obtain the CMM images. Different threshold values of the correlation coefficient allow a different number of multistatic radar signals to be included in the image formation process. It can be observed from Fig. 7b that the minimum value of S/C is produced by using only monostatic signals in the imaging process whereas S/C is greatly improved by including a number of multistatic signals. A threshold value of 0.91 allows inclusion of 48 multistatic signals of the form $b_{(i,i+k)}$ and $b_{(i+k,i)}$ (where $k = 1$). The addition

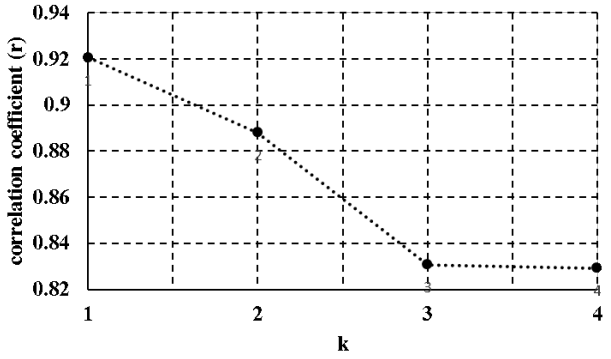

(a)

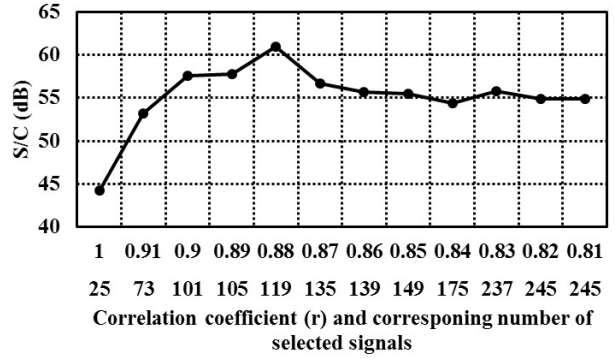

(b)

Figure 7: (a) Correlation coefficient r obtained by correlating $D[n]$ of monostatic signals group with $D[n]$ of multistatic signal groups ($b_{(i,i+k)}$ where $k = 1, 2, 3, 4$), (b) S/C as a function of the number of signals selected for the imaging process and the value of correlation coefficient r used as threshold for signal selection.

of 48 multistatic to the 25 monostatic signals (total 73 signals) results in the improvement of S/C ratio from approximately 44dB to 54dB.

Further relaxing the threshold value allows more multistatic signals to be used in the imaging process which further improves the S/C ratio. Peak S/C is achieved at a threshold value of 0.88 allowing 119 multistatic signals to be used in the image formation process. There is no advantage in using any additional multistatic signals. These additional signals may reduce the image quality as shown in the Fig. 7b at a threshold value of 0.82. It should also be noted that a significant improvement in S/C is achieved compared to the monostatic signals with a threshold value as high as 0.90. Therefore, using a higher value for the threshold would still improve the S/C compared to using monostatic signals alone.

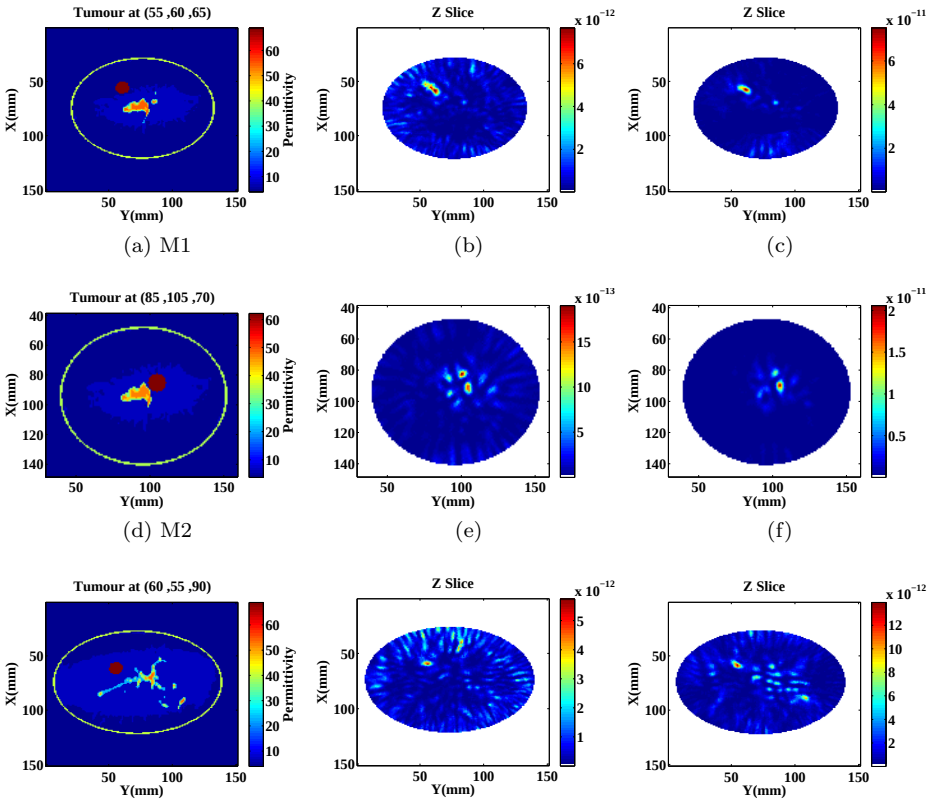

(a) M1 (b) (c)

(d) M2 (e) (f)

(g) M3 (h) (i)

Figure 8: Coronal view of FDTD breast models (a,d,g) showing permitivity of the breast tissues computed at the center frequency of the pulse, corresponding monostatic beamformed images (b,e,h), and corresponding CMM images (c,f,i).

The algorithm is then applied to the heterogeneous breast models in order to evaluate the robustness and the effectiveness of the algorithm in presence of realistic heterogeneity and fibroglandular tissues.

Fig. 8-10 show the coronal view of all FDTD breast models and the corresponding beamformed images following the application of the proposed artifact removal algorithm. The improvement in image quality can be observed by comparing the monostatic and the CMM beamformed images in each figure. In particular, the advantage of the CMM imaging is illustrated in images of the breast model M5. The monostatic imaging fails to localize the tumour due to limited monostatic data as shown in Fig. 9e. However, the tumour can be detected with small localization error in the CMM image when multistatic data is also used in addition to the monostatic signals (Fig. 9f).

The localization error in the images with higher density of fibroglandular tissues can be largely attributed to the imaging algorithm that uses the assumed

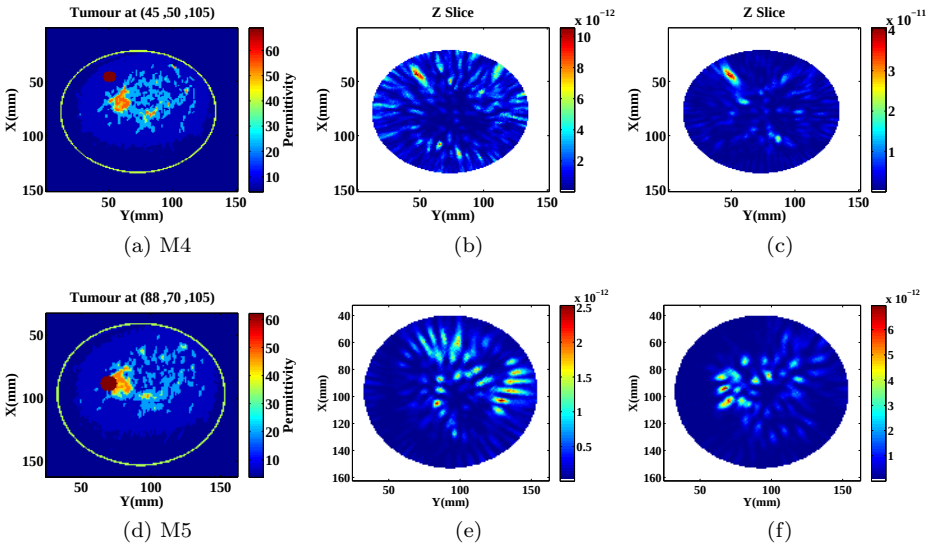

(a) M4 (b) (c)

(d) M5 (e) (f)

Figure 9: Coronal view of FDTD breast models (a,d) showing permittivity of the breast tissues computed at the center frequency of the pulse, corresponding monostatic beamformed images (b,e), and corresponding CMM images (c,f).

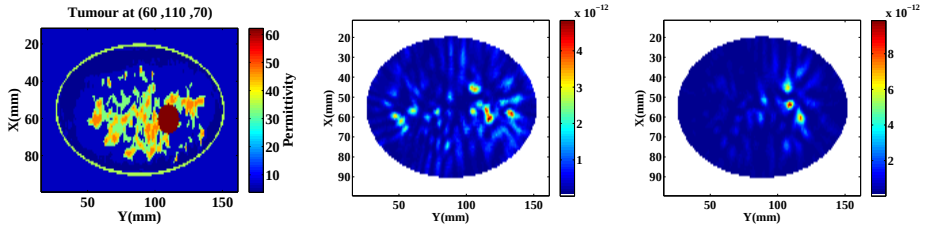

(a) M6 (b) (c)

Figure 10: (a) Coronal view of FDTD breast model (M6) showing permittivity of the breast tissues computed at the center frequency of the pulse, (b) corresponding monostatic beamformed image, (c) and corresponding CMM image.

constant propagation velocity of the microwave signals during image reconstruction process. The tumour localization can be improved by estimating the average relative permitivity of the breast using time of flight measurements [13], transmission measurement system [14] or by integrating the 3D permitivity model of the breast as a-priori information into the imaging algorithm [15].

Table 2 illustrates performance of the CMM imaging in terms of PPRR, S/M and S/C. The images are obtained using the proposed artifact removal algorithm and a GPU accelerated version of MDAS beamforming algorithm [16]. The metrics are computed for each individual heterogeneous breast phantom and tumour location used to evaluate the algorithm. Similar metrics have also been

computed for monostatic images.

Table 2: Performance metrics for the raw signals and the beamformed images

Breast Model	Signal Type	Selected Signals	S/C (dB)	S/M (dB)	PPRR (dB)
M1	Monostatic	25	1.48	23.54	-169.45
	Multistatic	73	3.72	28.62	-152.48
M2	Monostatic	25	5.63	34.46	-213.98
	Multistatic	109	12.71	48.29	-203.00
M3	Monostatic	25	5.57	26.52	-172.65
	Multistatic	83	10.02	38.51	-160.13
M4	Monostatic	40	1.78	21.95	-173.16
	Multistatic	116	6.78	29.50	-154.23
M5	Monostatic	50	-13.90	14.48	-212.37
	Multistatic	289	2.95	33.90	-198.36
M6	Monostatic	50	0.87	27.17	-215.63
	Multistatic	278	4.16	37.28	-210.16
Average	Monostatic		3.06	24.69	-192.87
	Multistatic		6.74	32.21	-179.73

Analyzing Table 2, the multistatic artifact removal followed by the CMM image formation process has shown an average improvement of over 50% in S/C and 23% in S/M, when compared to monostatic images. However, the PPRR value of the proposed alogrithm is slightly poorer than the monostatic HAR algorithm, as would be expected due to the greater variation in early-stage artifacts in multistatic radar signals. However, improvements in S/C and S/M values clearly indicate that residual artifacts have a negligible effect on the beamformed images. Overall, the CMM imaging supported by the proposed artifact removal algorithm consistently outperforms monostatic imaging.

5. Conclusions and Future Work

In this study, a novel adaptive multistatic artifact removal algorithm for microwave breast imaging applications is presented, which extends the monostatic HAR algorithm. Multistatic signals with similar early-stage artifacts are grouped together and an entropy-based method is used to adaptively select useful signal groups that will improve the imaging quality. The selected multistatic signal groups are then separately processed through the HAR algorithm in order to remove the artifact from the multistatic signals. The artifact-free signals are then used in beamforming to produce improved breast images compared to their monostatic equivalent.

The CMM images obtained after application of multistatic artifact removal are compared with the monostatic images. Results indicate that higher quality

multistatic images can be obtained after application of the proposed artifact removal algorithm, from simple homogeneous to more realistic dielectrically heterogeneous scenarios.
Future work will focus on the evaluation of the proposed alogrithm with other data-independent beamformers.

6. Acknowledgment

This work is supported by Science Foundation Ireland (Grant Numbers: 11/SIRG/I2120 and 12/IP/1523) and has been developed in the framework of COST Action TD1301, MiMed.

References

[1] S. C. Hagness, A. Taflove, J. E. Bridges, L. Fellow, Two-Dimensional FDTD Analysis of a Pulsed Microwave Confocal System for Breast Cancer Detection : Fixed-Focus and Antenna-Array Sensors, Biomedical Engineering, IEEE Transactions on 45 (12) (1998) 1470–1479.

[2] M. A. Elahi, M. Glavin, E. Jones, M. O'Halloran, Artifact removal algorithms for microwave imaging of the breast, Progress In Electromagnetics Research 141 (May) (2013) 185–200.

[3] M. A. Elahi, A. Shahzad, M. Glavin, E. Jones, M. O'Halloran, Hybrid Artifact Removal for Confocal Microwave Breast Imaging, IEEE Antennas and Wireless Propagation Letters 13 (2014) 149–152. doi:10.1109/LAWP.2014.2298975.

[4] M. Klemm, I. J. Craddock, A. Preece, J. Leendertz, R. Benjamin, Evaluation of a hemi-spherical wideband antenna array for breast cancer imaging, Radio Science 43 (6) (2008) RS6S06. doi:10.1029/2007RS003807.

[5] M. Helbig, M. Kmec, J. Sachs, C. Geyer, I. Hilger, G. Rimkus, Aspects of antenna array configuration for UWB breast imaging, in: Proceedings of 6th European Conference on Antennas and Propagation, EuCAP 2012, 2012, pp. 1737–1741. doi:10.1109/EuCAP.2012.6206594.

[6] M. O'Halloran, E. Jones, M. Glavin, Quasi-Multistatic MIST Beamforming for the Early Detection of Breast Cancer, IEEE Transactions on Biomedical Engineering 57 (4) (2010) 830–840. doi:10.1109/TBME.2009.2016392.

[7] W. Zhi, F. Chin, M. Chia, Near field uwb lcmv imaging for breast cancer detection with entropy based artifacts removal, in: IEEE Int. Conf. Acoust. Speech Signal Proc. (ICASSP), 2006, pp. II–577–II–580. doi:10.1109/ICASSP.2006.1660408.

[8] R. G. Baraniuk, S. Member, P. Flandrin, A. J. E. M. Janssen, O. J. J. Michel, Measuring Time Frequency Information Content Using the Rényi Entropies, IEEE Transactions on Information Theory 47 (4) (2001) 1391–1409.

[9] W. Zhi, F. Chin, Entropy-Based Time Window for Artifact Removal in UWB Imaging of Breast Cancer Detection, IEEE Signal Processing Letters 13 (10) (2006) 585–588. doi:10.1109/LSP.2006.876346.

[10] E. Zastrow, S. Davis, M. Lazebnik, Database of 3d grid-based numerical breast phantoms for use in computational electromagnetics simulations (2008).
URL `http://uwcem.ece.wisc.edu/home.htm`

[11] M. Lazebnik, D. Popovic, L. McCartney, C. B. Watkins, M. J. Lindstrom, J. Harter, S. Sewall, T. Ogilvie, A. Magliocco, T. M. Breslin, W. Temple, D. Mew, J. H. Booske, M. Okoniewski, S. C. Hagness, A large-scale study of the ultrawideband microwave dielectric properties of normal, benign and malignant breast tissues obtained from cancer surgeries., Physics in medicine and biology 52 (20) (2007) 6093–115. doi:10.1088/0031-9155/52/20/002.

[12] M. Klemm, J. A. Leendertz, D. Gibbins, I. J. Craddock, A. Preece, R. Benjamin, Microwave Radar-Based Breast Cancer Detection : Imaging in Inhomogeneous Breast Phantoms, IEEE Antennas and Wireless Propagation Letters 8 (2010) 1349–1352.

[13] M. Sarafianou, I. J. Craddock, T. Henriksson, M. Klemm, D. R. Gibbins, A. W. Preece, J. A. Leendertz, R. Benjamin, MUSIC Processing for Permittivity Estimation in a Delay-And-Sum Imaging System, in: Antennas and Propagation (EuCAP), 2013 7th European Conference on, 2013, pp. 821–824.

[14] J. Bourqui, E. C. Fear, Dielectric Permittivity Estimation of Biological Tissues using Sensor Array Technology, RF and Wireless Technologies for Biomedical and Healthcare Applications (IMWS-BIO), 2015 IEEE MTT-S 2015 International Microwave Workshop Series on (2015) 125—-126.

[15] J. Moll, T. Kelly, D. Byrne, M. Sarafianou, Microwave Radar Imaging of Heterogeneous Breast Tissue Integrating A-Priori Information, International Journal of Biomedical Imaging 2014 (2014) 17.

[16] M. A. Elahi, A. Shahzad, M. Glavin, E. Jones, M. O'Halloran, GPU accelerated Confocal microwave imaging algorithms for breast cancer detection, Antennas and Propagation (EuCAP), 2015 9th European Conference on (2015) 1–2.